Voltage-Calcium Coupling in the Genesis of Early and Delayed Afterdepolarizations in Cardiac Myocytes

Zhen Song, Christopher Y. Ko, Michael Nivala, James N. Weiss, Zhilin Qu

Supplemental Methods

A. Myocyte experiments

Myocyte Isolation. Mouse ventricular myocytes were isolated enzymatically as described previously (2). Briefly, C57Bl/6 mice (6-8 weeks) were injected intraperitoneally with 800 μl heparin (5,000 units/ml) 20-30 minutes before anesthetization and sacrifice with isoflurane (Phoenix Pharmaceuticals, Inc.). Hearts were quickly excised by thoracotomy and retrogradely perfused on a Langendorff apparatus maintained at 37°C. Enzyme digestion step consisted of perfusing Tyrode's solution containing 1 mg/ml collagenase (Type II; Worthington) and 2.8 mg/ml protease (Type XIV, Sigma) for 13-15 minutes. Myocytes were separated from digested ventricles by gentle mechanical dissociation and used within 4-6 hours. The modified Tyrode's solution contained the following (mmol/L): 136 NaCl, 5.4 KCl, 0.33 NaH_2PO_4, 1.0 $MgCl_2$, 10 HEPES, and 10 glucose; pH 7.4 (KOH). All chemicals were purchased from Sigma unless indicated otherwise. All procedures comply with UCLA Animal Research Committee policies.

Patch Clamp Recordings. APs from isolated myocytes were recorded in the current clamp mode using the perforated patch technique with Amphotericin B (240 μg/ml), as previously described (6, 7). Borosilicate glass electrodes (tip resistance 1.5-3 MΩ) were filled with internal solution containing (in mmol/L) 110 K-Aspartate, 30 KCl, 5 NaCl, 10 HEPES, 0.1 EGTA, 5 MgATP, 5 creatine phosphate, and 0.1 cAMP; pH 7.2 (KOH). The standard bath Tyrode's solution contained (in mmol/L): 136 NaCl, 5.4 KCl, 0.33 NaH_2PO_4, 1.0 $MgCl_2$, 10 HEPES, 1.8 $CaCl_2$, and 10 glucose; pH 7.4 (KOH). Extracellular [Ca] was raised to 2.7 mmol/L to facilitate EADs and DADs. APs were elicited with square current pulses of 2 ms duration and twice threshold amplitude. Data were acquired with an Axopatch 200A patch-clamp amplifier and Digidata 1200 acquisition board driven by pCLAMP 9.0 software (Axon Instruments, Inc.). Corrections were made for liquid junction potentials. Signals were filtered at 1 kHz. All experiments were carried out at 37°C.

Calcium Imaging. Myocytes were incubated with fluorescent Ca indicator dye Fluo-4 AM (10 μM, Life Technologies) and nonionic surfactant Pluronic F-127 (0.02%, Life Technologies) in Tyrode's solution for 30 minutes at room temperature before imaging. Ca fluorescence in isolated myocytes was recorded using an inverted Nikon Diaphot microscope (60X objective, Olympus) equipped with a charge-coupled device (CCD)-based Photometrics Cascade 128+ camera (~120 frames/s, 128 x 128 pixels) operating under Imaging Workbench software (version 6.0, INDEC BioSystems). Voltage was concurrently recorded in patch-clamped myocytes. Pseudo-line scan images were generated from the acquired video data using ImageJ software (11).

B. Rabbit ventricular cell model

1. The spatial structure of ventricular myocyte model

The ventricular myocyte model is a three-dimensional object containing 19,305 (65×27×11) CRUs (FIGURE) with CRU spacing being 1.84 μm in the longitudinal direction and 0.9 μm in the transverse direction, corresponding to a dimension 121 μm × 25 μm × 11 μm. The CRUs are coupled via Ca diffusion in the cytosolic space and SR. The model was modified from the one developed by Restrepo et al. (12). The details of the model are described in the sections below. Briefly, each CRU contains five sub-volumes with defined volume ratios (right panel in FIG.A): network SR (NSR), junctional SR (JSR), dyadic space (DS), sub-membrane space (SUB), and cytosolic space (CYTO). Ca from extracellular space enters into DS via LCCs and is released from the JSR to DS via RyRs. Each CRU has a cluster of 100 RyR channels associated with a cluster of 12 LCCs, both simulated using random Markov transitions. Ca is extruded from the SUB space via NCX and taken up into the NSR from CYTO via SERCA pump. Ca diffuses freely between the SR sub-volumes and between the cytosolic sub-volumes. CRUs are coupled via Ca diffusion between neighboring NSR spaces, SUB

spaces, and CYTO spaces, respectively. No Ca diffusion exists directly between neighboring JSR spaces or between neighboring DS spaces.

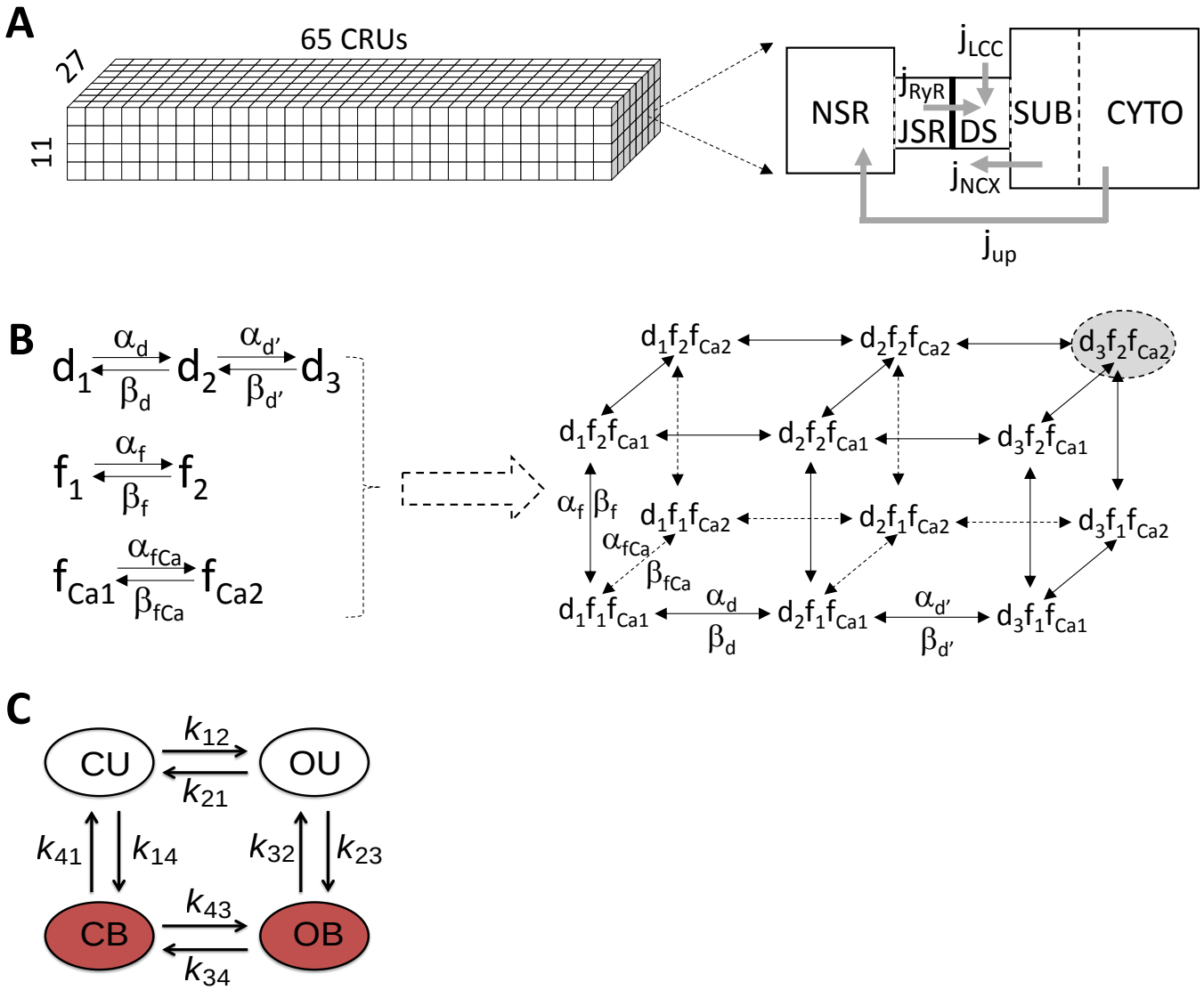

FIGURE. **Schematics of the computer AP/Ca cycling model**. **A**. Schematic diagrams of 3D structure of the cell model (left) and the CRU model (right). **B**. The modified $I_{Ca,L}$ model. Left: the Hodgkin-Huxley (HH) scheme. Right: the equivalent Markov scheme of the HH scheme. **C**. The 4-state RyR model.

However, a directly randomized version of the HH-type formulation is not appropriate for an LCC because the maximum open probability of an LCC is 100% in the HH-type model at high voltages, whereas that of real channels is much smaller (~5%). To reduce the open probability, we added a new state (d_3 in FIG.B) to the d gate of the HH-type model, with d_3 being the activated state. The transitions rates α_d, β_d, α_f, and β_f are the same as in the Luo and Rudy model (13). The rate constants for Ca-dependent inactivation were modified to account for the fact that Ca concentration in the DS space, which is much higher than the bulk cytosolic Ca concentration, was used to mediate LCC inactivation. The steady state of d_3 (the steady-state activation curve) is:

$$d_{3\infty} = \frac{\alpha_d}{\alpha_d + \frac{\beta_{d'}}{\alpha_{d'}}(\alpha_d + \beta_d)}$$

Since the open probability is small, i.e., $\frac{\beta_{d'}}{\alpha_{d'}} >> 1$, then $d_{3\infty} \approx \frac{\alpha_{d'}}{\beta_{d'}} \frac{\alpha_d}{\alpha_d + \beta_d}$, which is a rescale of the original model. Therefore, by shifting the voltage dependence of α_d and β_d or α_f and β_f, the window $I_{Ca,L}$ can be changed directly without affecting other properties of the channel. The right panel of FIG.B shows the equivalent Markov scheme of the LCC of the modified HH-type model.

2. Voltage and ionic currents

The differential equation for membrane voltage is

$$\frac{dV}{dt} = -\frac{1}{C_m}(I_{ion} + I_{stim})$$

where $C_m = 1\ \mu F/cm^2$ is the cell membrane capacitance, I_{stim} is the stimulus current pulse which was set as -40 $\mu A/cm^2$ and duration 1 ms, and I_{ion} is the total membrane current density, which is described by

$$I_{ion} = I_{Na} + I_{K1} + I_{Kr} + I_{Ks} + I_{to,f} + I_{to,s} + I_{NaK} + I_{Ca,L} + I_{NCX}$$

The mathematical formulations of the ionic currents are detailed in following sub-sections and their conductance are listed in Table S1. The physical constants and ion concentrations are listed in Table S2.

Table S1. Ionic current conductance

Parameter	Description	Value
g_{Na}	I_{Na} conductance	12.0 mS/μF
$g_{to,f}$	$I_{to,f}$ conductance	0.11 mS/μF
$g_{to,s}$	$I_{to,s}$ conductance	0.04 mS/μF
g_{K1}	I_{K1} conductance	0.3 mS/μF
g_{Kr}	I_{Kr} conductance	0.0125 mS/μF
g_{Ks}	I_{Ks} conductance	0.1386 mS/μF
g_{Nak}	I_{NaK} conductance	1.5 mS/μF

Table S2. Physical constants and ionic concentrations

Parameter	Description	Value
F	Faraday constant	96.5 C/mmol
R	Universal gas constant	8.315 $Jmol^{-1}K^{-1}$
T	Temperature	308 K
$[Na]_o$	External sodium concentration	136 mM
$[K]_o$	External potassium concentration	5.4 mM
$[K]_i$	Internal potassium concentration	140 mM
$[Ca]_o$	External calcium concentration	1.8 mM

2.1. Sodium current (I_{Na})

$$I_{Na} = g_{Na} m^3 hj(V - E_{Na}),$$

$$E_{Na} = \frac{RT}{F} \ln\left(\frac{[Na]_o}{[Na]_i}\right),$$

$$\frac{dh}{dt} = \alpha_h(1-h) - \beta_h h,$$

$$\frac{dj}{dt} = \alpha_j(1-j) - \beta_j j,$$

$$\frac{dm}{dt} = \alpha_m(1-m) - \beta_m m,$$

$$\alpha_m = 0.32\frac{V+47.13}{1-e^{-0.1(V+47.13)}},$$
$$\beta_m = 0.08e^{-\frac{V}{11}},$$

For $V \geq -40\ mV$,

$$\alpha_h = 0,$$
$$\alpha_j = 0,$$
$$\beta_h = \frac{1}{0.13\left(1+e^{\frac{V+10.66}{-11.1}}\right)},$$
$$\beta_j = 0.3\frac{e^{-2.535\times10^{-7}V}}{1+e^{-0.1(V+32)}},$$

For $V \leq -40\ mV$,

$$\alpha_h = 0.135e^{\frac{V+80}{-6.8}},$$
$$\beta_h = 3.56e^{0.079V} + 3.1\times10^5 e^{0.35V},$$
$$\alpha_j = \frac{(-127140e^{0.2444V} - 0.03474e^{-0.04391V})\times(V+37.78)}{1+e^{0.311(V+79.23)}},$$
$$\beta_j = \frac{0.1212e^{-0.01052V}}{1+e^{-0.1378(V+40.14)}}.$$

2.2. L-type Ca channel model and whole-cell $I_{Ca,L}$

The Ca channel model was modified as described in detail in Section 1. The opening of individual LCCs is simulated by a stochastic 12-state Markov model (panel B in FIGURE). Each CRU is assumed to have N_L LCCs under control condition. The Ca flux into the proximal space (dyadic space) of a CRU (the (m, n, k)th CRU in cell) is given by

$$\bar{I}_{Ca,L}(m,n,k) = i_{Ca,L}(m,n,k)L(m,n,k),$$

where $L \leq N_L$ is the number of open LCCs in the CRU, and $i_{Ca,L}$ is the single channel current of the CRU which is:

$$i_{Ca,L}(m,n,k) = \frac{4P_{Ca}zF\left(\gamma_i\, c_p(m,n,k)e^{2z} - \gamma_o[Ca]_o\right)}{e^{2z}-1},$$
$$z = \frac{VT}{RT}.$$

c_p(m,n,k) is the Ca concentration in the corresponding proximal space of the CRU. Therefore, the whole-cell L-type Ca current ($I_{Ca,L}$) is summation of the Ca currents of CRUs in the cell, i.e.,

$$I_{Ca,L} = \sum_{m,n,k=1}^{M,N,K} \bar{I}_{Ca,L}(m,n,k)$$

where M, N, and K are the dimensions of the CRU network forming the cell.

The transition rates between different states of the LCC model are:

$$\alpha_d = \frac{d_\infty}{\tau_d}, \qquad \beta_d = \frac{1-d_\infty}{\tau_d}$$

where

$$d_\infty = \frac{1}{1+e^{-\frac{V-5}{6.24}}},$$
$$\tau_d = \frac{1-e^{-\frac{V-5}{6.24}}}{0.035(V-5)}\, d_\infty.$$

$$\alpha_f = \frac{f_\infty}{\tau_f}, \qquad \beta_f = \frac{1 - f_\infty}{\tau_f}$$

where

$$f_\infty = \frac{1}{1 + e^{\frac{V+32.06}{8.6}}},$$

$$\tau_f = \frac{1}{0.0197e^{-[0.0337(V+7)]^2} + 0.02}.$$

$$\alpha_{fCa} = \frac{f_{Ca\infty}}{\tau_{fCa}}, \qquad \beta_{fCa} = \frac{1 - f_{Ca\infty}}{\tau_{fCa}}$$

where

$$f_{Ca\infty} = \frac{1}{1 + \left(\frac{c_p}{\bar{c}_p}\right)^2}.$$

$\alpha_{d'}$ and $\beta_{d'}$ are constants (Table S3). The parameters are listed in Table S3.

Table S3. L-type Ca current parameters

Parameter	Description	Value
P_{Ca}	L-type channel permeability	11.9 μmolC^{-1}ms^{-1}
γ_i, γ_o	Activity coefficient of Ca	0.341
N_L	Number of LCCs in each CRU	12
$\bar{c}_p$	Threshold of Ca-dependent inactivation	6 μM
τ_{fCa}	Time constant of Ca-dependent inactivation	15 ms
$\alpha_{d'}$	Transition rate from d_2 to d_3	0.3 ms^{-1}
$\beta_{d'}$	Transition rate from d_3 to d_2	6 ms^{-1}

2.3. Sodium-calcium exchange current (I_{NCX})

The Na-Ca exchange are spatially distributed in the CRUs, which are functions of Ca concentrations of the local sub-membrane spaces (c_s). For the (m,n,k)th CRU, the Na-Ca change current is:

$$\bar{I}_{NCX}(m,n,k) = \frac{K_a \nu_{NaCa}\left(e^{\eta z}[Na]_i[Ca]_o - e^{(\eta-1)z}[Na]_o^3 c_s(m,n,k)\right)}{(t_1 + t_2 + t_3)(1 + k_{sat}e^{(\eta-1)z})},$$

where

$$t_1 = K_{mCai}\,[Na]_o^2\left[1 + \left(\frac{[Na]_i}{K_{mNai}}\right)^3\right],$$

$$t_2 = K_{mNao}^3 c_s(m,n,k)(1 + \frac{c_s(m,n,k)}{K_{mCai}})$$

$$t_3 = K_{mCao}^3[Na]_i^3 + [Na]_i^3[Ca]_o + [Na]_o^3 c_s(m,n,k),$$

$$K_a = \left[1 + \left(\frac{K_{da}}{c_s(n,m,k)}\right)^3\right]^{-1},$$

$$z = \frac{VF}{RT},$$

and the whole-cell I_{NCX} is:

$$I_{NCX} = \sum_{m,n,k=1}^{M,N,K} \bar{I}_{NCX}(m,n,k)$$

The parameters are listed in Table S4.

Table S4. Sodium-calcium exchange current parameters

Parameter	Value	Units
v_{NaCa}	7	μM ms^{-1}
$\mathrm{K_{mCai}}$	3.59	μM
$\mathrm{K_{mCao}}$	1.3	mM
$\mathrm{K_{mNai}}$	12.3	mM
$\mathrm{K_{mNao}}$	87.5	mM
$\mathrm{K_{da}}$	0.11	μM
$\mathrm{k_{sat}}$	0.27	
η	0.35	

2.4. Inward rectifier K current (I_{K1})

$$I_{K1} = g_{K1}\sqrt{\frac{[K]_o}{5.4}}\,\frac{A_{K1}}{A_{K1}+B_{K1}}(V-E_K),$$

$$A_{K1} = \frac{1.02}{1+e^{0.2385(V-E_K-59.215)}},$$

$$B_{K1} = \frac{0.49124e^{0.08032(V-E_K+5.476)} + e^{0.06175(V-E_K-594.31)}}{1+e^{-0.5143(V-E_K+4.753)}},$$

$$E_K = \frac{RT}{F}\ln\left(\frac{[K]_o}{[K]_i}\right).$$

2.5. The rapid component of the delayed rectifier K current (I_{Kr})

$$I_{Kr} = g_{Kr}\sqrt{\frac{[K]_o}{5.4}}\,x_{Kr}R(V)(V-E_K),$$

$$R(V) = \frac{1}{1+e^{\frac{V+33}{22.4}}},$$

$$\frac{dx_{Kr}}{dt} = \frac{x_{Kr}^{\infty}-x_{Kr}}{\tau_{Kr}},$$

$$x_{Kr}^{\infty} = \frac{1}{1 + e^{-\frac{V+50}{7.5}}},$$

$$\tau_{Kr} = \frac{1}{\frac{0.00138(V+7)}{1 - e^{-0.123(V+7)}} + \frac{0.00061(V+10)}{-1 + e^{0.145(V+10)}}},$$

2.6. The slow component of the delayed rectifier K current (I_{Ks})

$$I_{Ks} = g_{Ks} x_{s1} x_{s2} q_{Ks} (V - E_{Ks}),$$
$$q_{Ks} = 1 + \frac{0.8}{1 + \left(\frac{0.5}{c_i}\right)^3},$$

$$\frac{dx_{s1}}{dt} = \frac{x_s^{\infty} - x_{s1}}{\tau_{xs1}},$$

$$\frac{dx_{s2}}{dt} = \frac{x_s^{\infty} - x_{s2}}{\tau_{xs2}},$$

$$x_s^{\infty} = \frac{1}{1 + e^{-\frac{V-1.5}{16.7}}},$$

$$\tau_{xs1} = \frac{1}{\frac{0.0000719(V+30)}{1 - e^{-0.148(V+30)}} + \frac{0.00031(V+30)}{-1 + e^{0.0687(V+30)}}},$$

$$\tau_{xs2} = 4\tau_{xs1},$$

$$E_{Ks} = \frac{RT}{F} \ln\left(\frac{[K]_o + 0.01833[Na]_o}{[K]_i + 0.01833[Na]_i}\right).$$

2.7. The fast component of the outward K current ($I_{to,f}$)

$$I_{to,f} = g_{to,f} X_{to,f} Y_{to,f} (V - E_K),$$
$$X_{to,f}^{\infty} = \frac{1}{1 + e^{-\frac{V+3}{15}}},$$

$$Y_{to,f}^{\infty} = \frac{1}{1 + e^{\frac{V+33.5}{10}}},$$

$$\tau_{Xto,f} = 3.5 e^{-\left(\frac{V}{30}\right)^2} + 1.5,$$
$$\tau_{Yto,f} = \frac{20}{1 + e^{\frac{V+33.5}{10}}} + 20,$$

$$\frac{dX_{to,f}}{dt} = \frac{X_{to,f}^{\infty} - X_{to,f}}{\tau_{Xto,f}},$$

$$\frac{dY_{to,f}}{dt} = \frac{Y_{to,f}^{\infty} - Y_{to,f}}{\tau_{Yto,f}}.$$

2.8. The slow component of the outward K current ($I_{to,s}$)

$$I_{to,s} = g_{to,s} X_{to,s}\left(Y_{to,s} + 0.5R_s^{\infty}\right)(V - E_K),$$

$$R_s^{\infty} = \frac{1}{1 + e^{\frac{V+33.5}{10}}},$$

$$X_{to,s}^{\infty} = \frac{1}{1 + e^{-\frac{V+3}{15}}},$$

$$Y_{to,s}^{\infty} = \frac{1}{1 + e^{\frac{(V+33.5)}{10}}},$$

$$\tau_{Xto,s} = \frac{9}{1 + e^{\frac{V+3}{15}}} + 0.5,$$

$$\tau_{Yto,s} = \frac{3000}{1 + e^{\frac{V+60}{10}}} + 30,$$

$$\frac{dX_{to,s}}{dt} = \frac{X_{to,s}^{\infty} - X_{to,s}}{\tau_{Xto,s}},$$

$$\frac{dY_{to,s}}{dt} = \frac{Y_{to,s}^{\infty} - Y_{to,s}}{\tau_{Yto,s}}.$$

2.9. Sodium-potassium pump current (I_{NaK})

$$\sigma = \frac{e^{\frac{[Na]_o}{67.3}} - 1}{7},$$

$$f_{NaK} = \frac{1}{1 + 0.1245e^{-\frac{0.1VF}{RT}} + 0.0365\sigma e^{-\frac{VF}{RT}}},$$

$$I_{NaK} = g_{NaK} f_{NaK} \frac{1}{1 + \frac{12}{[Na]_i}} \times \frac{[K]_o}{[K]_o + 1.5}.$$

3. Intracellular Ca cycling

3.1. Differential equations for Ca cycling

The Ca cycling are described by the following differential equations [for an arbitrary CRU at a location (m,n,k) with the spatial location omitted in the equations]:

$$\frac{dc_i}{dt} = \beta_i(c_i)\left(I_{dsi}\frac{v_s}{v_i} - I_{up} + I_{leak} - I_{TCi} + I_{ci}\right),$$
$$\frac{dc_s}{dt} = \beta_s(c_s)\left(I_{dps}\frac{v_p}{v_s} + I_{NCX} - I_{dsi} - I_{TCs} + I_{cs}\right),$$
$$\frac{dc_p}{dt} = \beta_p(c_p)\left(I_{rel} + I_{Ca,L} - I_{dps}\right),$$
$$\frac{dc_{nsr}}{dt} = \left(I_{up} - I_{leak}\right)\frac{v_i}{v_{nsr}} - I_{tr}\frac{v_{jsr}}{v_{nsr}} + I_{cnsr},$$
$$\frac{dc_{jsr}}{dt} = \beta_{jsr}(c_{jsr})\left(I_{tr} - I_r\frac{v_p}{v_{jsr}}\right),$$

where c_i is the free Ca concentration in the bulk myoplasm, c_s is the free Ca concentration in a thin layer just below the cell membrane, c_p is the free Ca concentration in the proximal space (dyadic space), c_{jsr} is the free Ca concentration in the junctional SR, c_{nsr} is the free Ca concentration in the network SR, β terms account for instantaneous buffer in corresponding compartments using the rapid buffering approximation, I_{up} is the SERCA uptake current representing total flux into the NSR, I_{leak} is the leak current from NSR to cytosol, I_{NCX} is Na-Ca exchange current, $I_{Ca,L}$ is the L-type Ca influx, I_{rel} is the total Ca efflux from the JSR, I_{dsi}, I_{dps} and I_{tr} are the diffusion currents from adjacent compartments, I_{TCi} and I_{TCs} are the troponin C dynamic buffering currents in cytosol and submembrane spaces, I_{ci}, I_{cs} and I_{cnsr} are the diffusive currents between neighboring CRUs in the corresponding compartments. Note that currents are all local currents for a single CRU, for example, $I_{Ca,L}$ is the same as $\bar{I}_{Ca,L}(m,n,k)$ and I_{NCX} the same as $\bar{I}_{NCX}(m,n,k)$ in the expressions of the whole-cell currents described in the sections of ionic currents. The values of compartments volumes are listed in Table S5.

Table S5. Effective volumes of sub-space of a CRU

Parameter	Description	Value
v_i	Cytosolic volume	0.5 μm^3
v_s	Submembrane space volume	0.025 μm^3
v_p	Proximal space volume	0.00126 μm^3
v_{jsr}	JSR volume	0.02 μm^3
v_{nsr}	NSR volume	0.025 μm^3

3.2. Instantaneous cytosolic buffering

The factors $\beta_i(c_i)$ and $\beta_s(c_s)$ describe instantaneous buffering to Calmodulin, SR sites, Myosin (Ca^{2+}), and Myosin (Mg^{2+}). Note that the concentration of the proximal space rapidly equilibrates, so we do not require knowledge of the instantaneous buffers in the proximal space. The equation of $\beta_i(c_i)$ is

$$\beta_i(c_i) = \left[1 + \frac{\sum B_b K_b}{(c_i + K_b)^2}\right]^{-1},$$

where the sum is over the instantaneous cytosolic buffers Calmodulin, SR sites, Myosin (Ca^{2+}), and Myosin (Mg^{2+}), with buffer dissociation constants K_{CAM}, K_{SR}, K_{MCa}, and K_{MMg} and total concentration of buffering sites B_{CAM}, B_{SR}, B_{MCa}, and B_{MMg}, respectively. In addition to Calmodulin, instantaneous buffering in the submembrane space includes the subsarcolemmal sites of high affinity with total

concentration of sites and dissociation constant B_{SLH} and K_{SLH}, respectively. The parameters for instantaneous cytosolic buffering are in Table S6.

Table S6. Buffering parameters.

Parameter	Value	Units
K_{CAM}	7.0	μM
B_{CAM}	24.0	μM
K_{SR}	0.6	μM
B_{SR}	47.0	μM
K_{MCa}	0.033	μM
B_{MCa}	140.0	μM
K_{SLH}	0.3	μM
B_{SLH}	13.4	μM
B_T	70.0	μM
k_{on}^T	0.0327	(μM ms)$^{-1}$
k_{off}^T	0.0196	(ms)$^{-1}$

3.3. Troponin C buffering

I_{TCi} and I_{TCs} describe the rate of change in the concentration of Ca bound to Troponin C in the cytosolic and submembrane compartments, $[CaT]_i$ and $[CaT]_s$. These quantities satisfy

$$\frac{d[CaT]_i}{dt} = I_{TC_i},$$

with

$$I_{TC_i} = k_{on}^T c_i (B_T - [CaT]_i) - k_{off}^T [CaT]_i,$$

and analogous expressions apply for the submembrane compartments, replacing the subscript *i* by *s*. Here, k_{on}^T and k_{off}^T are the on- and off-rate constants for Ca Troponin C binding, and B_T is the total concentration of Troponin C buffering sites. The values of these parameters are listed in Table S6.

3.4. Instantaneous luminal buffering

$B_{jsr}(c_{jsr})$ describes instantaneous luminal Ca buffering to calsequestrin (CSQN). The expression of $\beta_{jsr}(c_{jsr})$ is

$$\beta(c) = \left(1 + \frac{K_c B_{CSQN} n(c) + \partial_c n(c)(cK_c + c^2)}{(K_c + c)^2}\right)^{-1},$$

where

$$n(c_{jsr}) = \widehat{M} n_M + (1 - \widehat{M}) n_D,$$

$$\widehat{M} = \frac{(1 + 8\rho B_{CSQN})^{\frac{1}{2}} - 1}{4\rho B_{CSQN}},$$

and

$$\rho(c_{jsr}) = \frac{\rho_\infty c_{jsr}^h}{K^h + c_{jsr}^h}.$$

The parameters for luminal buffering are in Table S7.

Table S7: Luminal buffering parameters.

Parameter	Description	Value
B_{CSQN}	Concentration of CSQN molecules	460 μM
K_C	Dissociation constant of CSQN	600 μM
n_M	Buffering capacity of CSQN monomers	15
n_D	Buffering capacity of CSQN dimers	35
ρ_∞	Asymptotic ratio of dimers to monomers	5000
K	Dimerization constant	850 μM
H	Dimerization exponent (steep)	23

3.5. SR Ca uptake current (I_{up})

$$I_{up} = \nu_{up}\left(\frac{\left(\frac{c_i}{K_i}\right)^H - \left(\frac{c_{nsr}}{K_{nsr}}\right)^H}{1 + \left(\frac{c_i}{K_i}\right)^H + \left(\frac{c_{nsr}}{K_{nsr}}\right)^H}\right).$$

The parameters are listed in Table S8.

Table S8. Uptake and leak current parameters.

Parameter	Value	Units
ν_{up}	0.3	μM ms^{-1}
K_i	0.3	μM
K_{NSR}	1700	μM
H	1.787	
g_{leak}	1.035×10^{-5}	ms^{-1}
K_{JSR}	500	μM

3.6. SR leak current (I_{leak})

$$I_{leak} = g_{leak}\left(\frac{c_{jsr}^2}{c_{jsr}^2 + K_{jsr}^2}\right)(c_{nsr} - c_i).$$

3.7. RyR release flux (I_{rel})

$$I_{rel} = J_{max}\, P_o\, \frac{c_{jsr} - c_p}{\nu_p},$$

where P_o is the fraction of RyR channels that are in the open state of RyRs. J_{max} is the maximum RyR flux strength. The parameters are listed in Table S9.

3.8. RyR model

The RyR model includes the following 4 states (Panel D in FIGURE): closed CSQN-unbound (CU), open CSQN-unbound (OU), open CSQN-bound (OB), and closed CSQN-bound (CB). The rates of transition are:

$$k_{12} = K_u c_p^2,$$

$$k_{14} = \frac{\widehat{M}\tau_b^{-1}B_{CSQN}}{B_{CSQN}^0},$$
$$k_{21} = \tau_c^{-1},$$
$$k_{23} = \frac{\widehat{M}\tau_b^{-1}B_{CSQN}}{B_{CSQN}^0},$$
$$k_{43} = K_b c_p^2,$$
$$k_{41} = \tau_u^{-1},$$
$$k_{34} = \tau_c^{-1},$$
$$k_{32} = \frac{k_{41}k_{12}}{k_{43}}.$$

The parameters are listed in Table S9. Note that B_{CSQN}/B_{CSQN}^0 is only different from 1 when the CSQN concentration is modified.

Table S9. SR release current and RyR model parameters

Parameter	Description	Value
J_{max}	Maximum RyR flux strength	1.47×10^{-2} $\mu m^3 ms^{-1}$
K_u	CSQN-unbound opening rate	3.8×10^{-4} $\mu M^{-2} ms^{-1}$
K_b	CSQN-bound opening rate	1×10^{-5} $\mu M^{-2} ms^{-1}$
τ_u	CSQN-unbinding timescale	700.0 ms
τ_b	CSQN-binding timescale	10.0 ms
τ_c	RyR closing timescale	1.0 ms
B_{CSQN}^0	Normal CSQN concentration	460 μM

3.9. Nearest-neighbor diffusive currents

The diffusive currents in cytosol, submembrane and NSR are given by

$$I_{ci}^{(n)} = \sum \left(\frac{c_i^{(m)} - c_i^{(n)}}{\tau_{mn}} \right),$$

where the sum is over the six nearest neighbors. The values of the timescales (τ_{mn}) are listed in Table S10.

Table S10: Parameters of Ca Diffusion

Parameter	Description	Value
τ_i^T	Transverse cytosolic	2.93 ms
τ_i^L	Longitudinal cytosolic	2.32 ms
τ_{nsr}^T	Transversal NSR	7.2 ms
τ_{nsr}^L	Longitudinal NSR	24.0 ms
τ_s^T	Transversal submembrane	1.42 ms
τ_s^L	Longitudinal submembrane	3.4 ms

C. Mouse ventricular cell model

We used the same spatial CRU structure and distribution as the rabbit ventricular cell model described above but substituted the ionic currents of mouse ventricular myocytes formulated by Morotti et al (5) except $I_{Ca,L}$ which was the same as in the rabbit ventricular cell model but a 65% increase in conductance, i.e.,

P_{Ca}=19.635 μmolC^{-1}ms^{-1}. The total ionic current is

$$I_{ion} = I_{Na} + I_{Na,L} + I_{Nabk} + I_{K1} + I_{Kr} + I_{to,f} + I_{NaK} + I_{Ca,L} + I_{Cabk} + I_{NCX} + I_{Kslow1} + I_{Kslow2} + I_{ss}$$

The details of the ionic currents are described below. The parameters are the same as in the Morotti et al unless specified.

Sodium current (I_{Na})

$$I_{Na} = g_{Na} m^3 hj(V - E_{Na}) ,$$

$$E_{Na} = \frac{RT}{F} \ln\left(\frac{[Na]_o}{[Na]_i}\right),$$

$$\frac{dh}{dt} = \alpha_h(1 - h) - \beta_h h ,$$

$$\frac{dj}{dt} = \alpha_j(1 - j) - \beta_j j ,$$

$$\frac{dm}{dt} = \alpha_m(1 - m) - \beta_m m ,$$

$$\alpha_m = 0.32 \frac{V + 47.13}{1 - e^{-0.1(V+47.13)}},$$

$$\beta_m = 0.08 e^{-\frac{V}{11}} ,$$

For $V \geq -40\ mV$,

$$\alpha_h = 0 ,$$

$$\alpha_j = 0 ,$$

$$\beta_h = \frac{0.66}{0.13\left(1 + e^{\frac{V+10.66}{-11.1}}\right)},$$

$$\beta_j = 0.3 \frac{e^{-2.535\times10^{-7}V}}{1 + e^{-0.1(V+32)}},$$

For $V \leq -40\ mV$,

$$\alpha_h = 0.135 e^{\frac{V+80}{-6.8}} ,$$

$$\beta_h = 3.92 e^{0.079(V-2)} + 3.1 \times 10^5 e^{0.35(V-2)} ,$$

$$\alpha_j = \frac{(-127140 e^{0.2444V} - 0.03474 e^{-0.04391V}) \times (V + 37.78)}{1 + e^{0.311(V+79.23)}},$$

$$\beta_j = \frac{0.1212e^{-0.01052V}}{1 + e^{-0.1378(V+40.14)}}.$$

Late sodium current ($I_{Na,L}$)

$$I_{Na,L} = g_{Na,L} m_L{}^3 h_L \left(V - E_{Na,L}\right),$$

$$E_{Na,L} = \frac{RT}{F} \ln\left(\frac{[Na]_o}{[Na]_i}\right),$$

$$h_{L,\infty} = \frac{1}{1 + \exp\left(\frac{V + 91}{6.1}\right)}$$

$$\tau_h = 4000\ ms$$

where m_L is the same as m in I_{Na}.

Background sodium current (I_{Nabk})

$$I_{Nabk} = g_{nabk}(V - E_{Na})$$

Inward rectifier potassium current (I_{K1})

$$I_{K1} = g_{K1} \sqrt{\frac{[K]_o}{5.4}}\ \frac{A_{K1}}{A_{K1} + B_{K1}} (V - E_K),$$

$$A_{K1} = \frac{1.02}{1 + e^{0.2385(V - E_K - 59.215)}},$$

$$B_{K1} = \frac{0.49124e^{0.08032(V - E_K + 5.476)} + e^{0.06175(V - E_K - 594.31)}}{1 + e^{-0.5143(V - E_K + 4.753)}},$$

$$E_K = \frac{RT}{F} \ln\left(\frac{[K]_o}{[K]_i}\right).$$

The rapid component of the delayed rectifier potassium current (I_{Kr})

$$I_{Kr} = g_{Kr} \sqrt{\frac{[K]_o}{5.4}}\ x_{Kr} R(V)(V - E_K),$$

$$R(V) = \frac{1}{1 + e^{\frac{V+33}{22.4}}},$$

$$\frac{dx_{Kr}}{dt} = \frac{x_{Kr}^{\infty} - x_{Kr}}{\tau_{Kr}},$$

$$x_{Kr}^{\infty} = \frac{1}{1 + e^{-\frac{V+50}{7.5}}},$$

$$\tau_{Kr} = \frac{1}{\frac{0.00138(V+7)}{1 - e^{-0.123(V+7)}} + \frac{0.00061(V+10)}{-1 + e^{0.145(V+10)}}},$$

The fast component of the transient outward potassium current ($I_{to,f}$)

$$I_{to,f} = g_{to,f} X_{to,f} Y_{to,f} (V - E_K),$$

$$X_{to,f}^{\infty} = \frac{1}{1 + e^{-\frac{V+3}{13}}},$$

$$Y_{to,f}^{\infty} = \frac{1}{1 + e^{\frac{V+48}{5}}},$$

$$\tau_{Xto,f} = 0.7e^{-\left(\frac{V+25}{30}\right)^2} + 0.08,$$

$$\tau_{Yto,f} = \frac{8}{1 + e^{\frac{V+60}{8}}} + 32e^{-\left(\frac{V+55}{16}\right)^2} + 10,$$

$$\frac{dX_{to,f}}{dt} = \frac{X_{to,f}^{\infty} - X_{to,f}}{\tau_{Xto,f}},$$

$$\frac{dY_{to,f}}{dt} = \frac{Y_{to,f}^{\infty} - Y_{to,f}}{\tau_{Yto,f}}.$$

Sodium-potassium pump current (I_{NaK})

$$\sigma = \frac{e^{\frac{[Na]_o}{67.3}} - 1}{7},$$

$$f_{NaK} = \frac{1}{1 + 0.1245e^{-\frac{0.1VF}{RT}} + 0.0365\sigma e^{-\frac{VF}{RT}}},$$

$$I_{NaK} = g_{NaK} f_{NaK} \frac{1}{1 + \frac{19}{[Na]_i}} \times \frac{[K]_o}{[K]_o + 1.5}.$$

L-type calcium current ($I_{Ca,L}$)

$I_{Ca,L}$ formulation is the same as in the rabbit ventricular cell model except that the activation kinetics is shifted to the negative voltage direction for 15 mV, i.e.,

$$d_\infty = \frac{1}{1+e^{-\frac{V+10}{6.24}}},$$

$$\tau_d = \frac{1-e^{-\frac{V+10}{6.24}}}{0.035(V+10)}\, d_\infty.$$

Background calcium leak current (I_{Cabk})

$$I_{Cabk} = g_{cabk}(V - E_{Ca})$$

Sodium-calcium exchange current (I_{NCX})

I_{NCX} formulation is the same as in the rabbit model with v_{NaCa}=3.6 pA/pF.

Slowly inactivating delayed rectifier potassium current ($I_{K,slow}$)

$$I_{kslow} = I_{kslow1} + I_{kslow2}$$

$$I_{kslow1} = g_{kslow1} x_{kslow1} y_{kslow1}(V - E_K)$$

$$I_{kslow2} = g_{kslow2} x_{kslow2} y_{kslow2}(V - E_K)$$

$$x_{kslowss} = \frac{1}{1+e^{\frac{V+15}{14}}}$$

$$\tau_{xkslow} = 0.95 + 0.05e^{-0.08V}$$

$$y_{kslowss} = \frac{1}{1+e^{\frac{V+48}{6.2}}}$$

$$\tau_{ykslow1} = 400 + 900e^{-\left(\frac{V+55}{16}\right)^2} - \frac{250}{1+e^{\frac{V+60}{8}}}$$

$$\tau_{ykslow2} = 400 + 900e^{-\left(\frac{V+55}{16}\right)^2} - \frac{550}{1+e^{\frac{V+60}{8}}}$$

$$\frac{dx_{kslow}}{dt} = \frac{x_{kslowss} - x_{kslow}}{\tau_{xkslow}},$$

$$\frac{dy_{kslow1}}{dt} = \frac{y_{kslowss} - y_{kslow1}}{\tau_{ykslow1}},$$

$$\frac{dy_{kslow2}}{dt} = \frac{y_{kslowss} - y_{kslow2}}{\tau_{ykslow2}},$$

where g_{Kslow1}=0.0352 nS/pF and g_{Kslow2}=0.028 nS/pF.

Non-inactivating steady-state current (I_{ss})

$$I_{ss} = g_{ss} x_{ss} (V - E_K),$$

where

$$x_{ssss} = x_{kslowss}$$

$$\tau_{xss} = 14 + 70e^{-\left(\frac{V+43}{30}\right)^2}$$

$$\frac{dx_{ss}}{dt} = \frac{x_{ssss} - x_{ss}}{\tau_{xss}}$$

D. Numerical methods

The differential equations for voltage and Ca concentrations of different compartments were numerically solved using an Euler method with a time step of 0.1 ms. The gating variables were integrated using the method by Rush and Larsen (14). The LCCs were simulated by a standard Monte Carlo method using the Markov model shown in FIGURE. The RyRs were simulated using an optimized method developed by Restrepo et al (12), which is equivalent to the binomial τ-leaping method (15). For all the simulations in this study, we pre-paced the cell model 50 beats to reach the steady state. All computer programs were coded in CUDA C, and simulations were carried out on a Graphical Processing Unit workstation with 2 intel Xeon E5-26640 processors and 4 Nvidia Tesla K20 GPUs. To simulate 1 s of electrical and Ca cycling activity, it takes ≈ 10 s of computational time.

Supplemental Figures

(Complex EAD behaviors observed in experiments from literature)

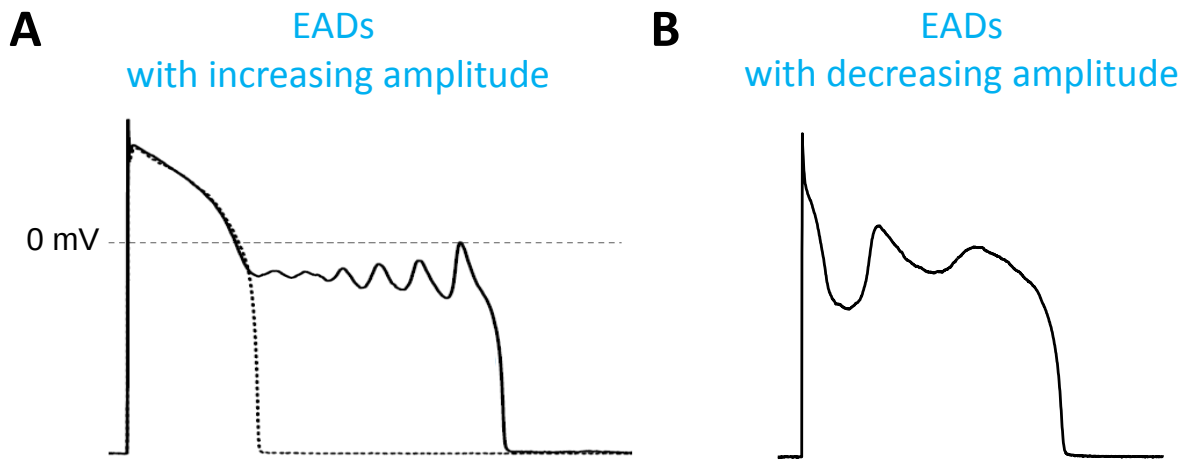

Fig.S1. **Complex EAD behaviors from experiments**. **A**. EADs with growing amplitude. From Liu et al (3). **B**. EADs with decreasing amplitude. From Xie et al (9).

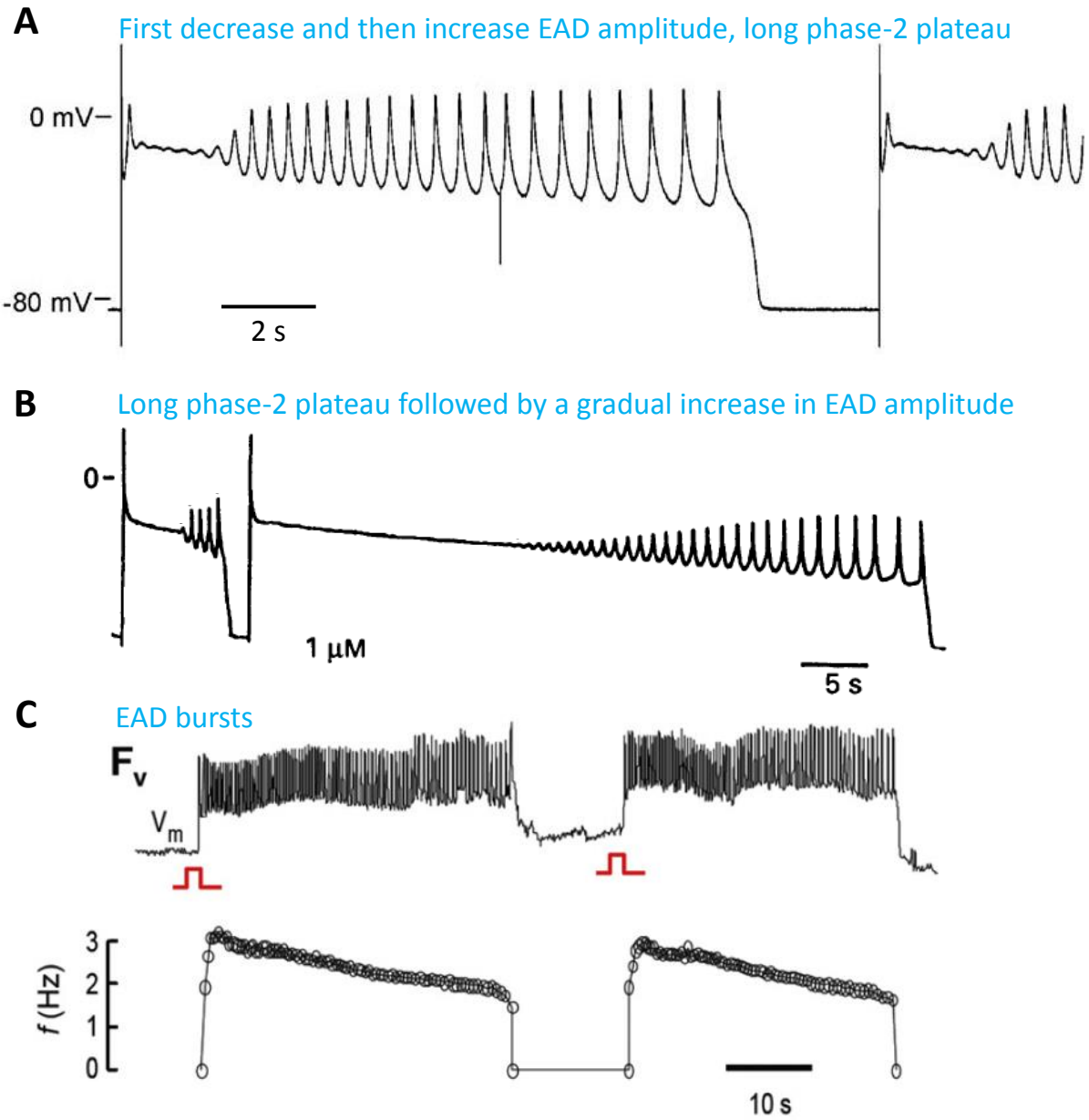

Fig.S2. Complex EAD behaviors from experiments. **A**. EADs with decreasing and then increasing amplitude and long phase-2 plateau. From Orth et al .(1). **B**. Long phase-2 plateau followed by EADs with growing amplitude. From Puisieux et al. (8). **C**. EAD bursts. Upper trace: optical voltage trace. Lower trace: Frequency of the EAD burst. From Change et al (10).

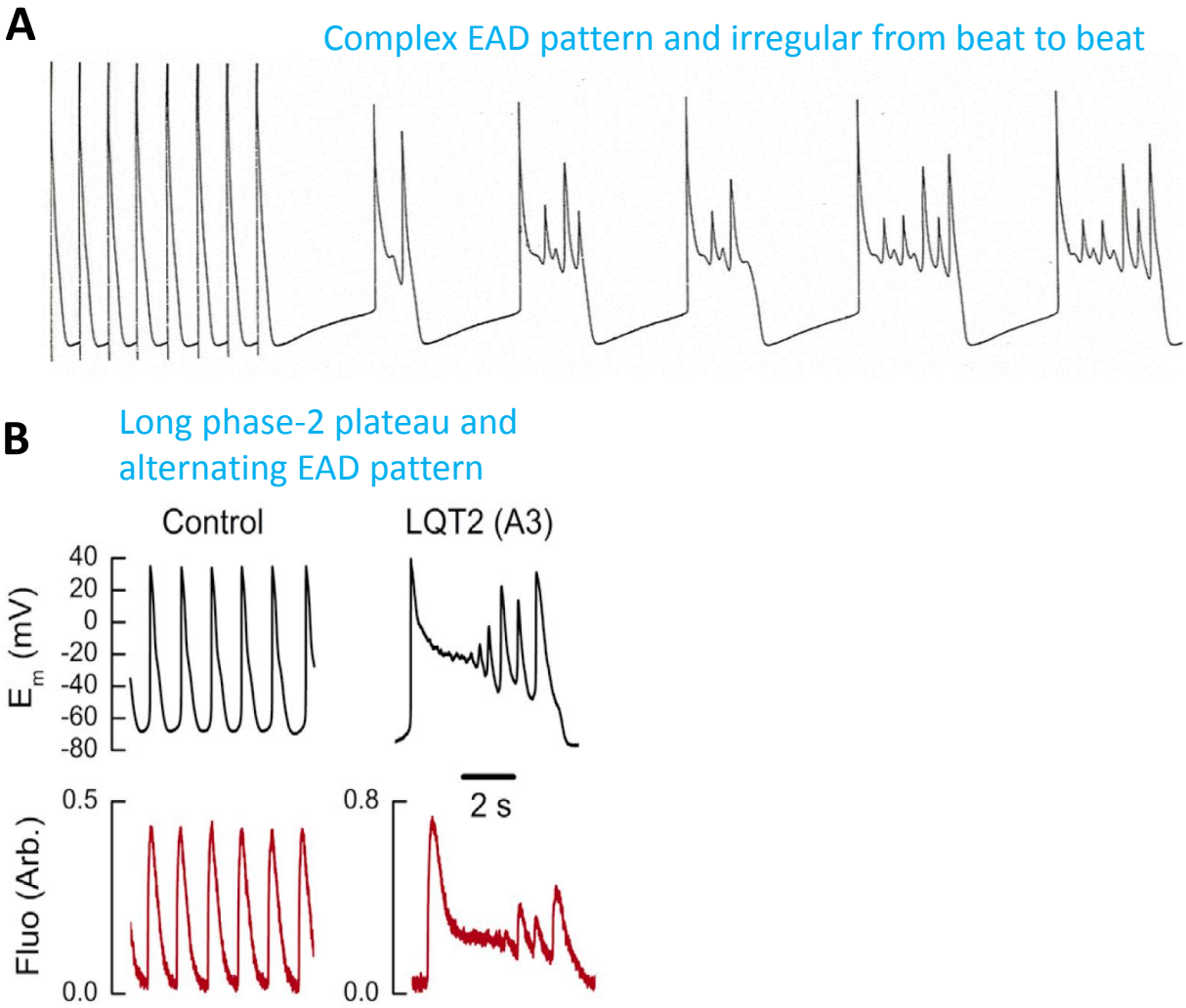

Fig.S3. Complex EAD behaviors from experiments. **A**. A recording from a dog Purkinje fiber showing complex EAD patterns and irregular beat-to-beat change (Courtesy of Robert Gilmour). **B.** Alternating EAD pattern following a long phase-2 plateau. During the phase-2 plateau, intracellular Ca is high without oscillation. From Spencer et al. (4).

Supplemental Results

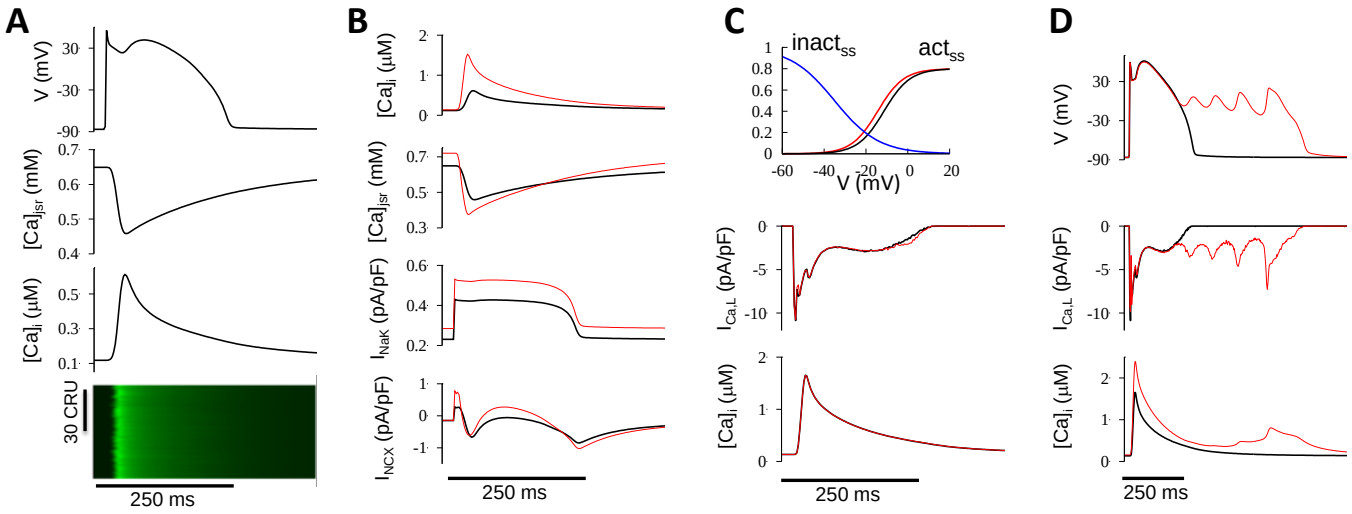

Fig. S4. **Model properties**. **A**. AP, $[Ca]_{SR}$, $[Ca]_i$, and a line scan of $[Ca]_i$ for the normal control model after steady state periodic pacing at PCL=2 s. **B**. $[Ca]_i$, $[Ca]_{SR}$, I_{NaK} and I_{NCX} for $[Na]_i$=7 mM (black) and 10 mM (red) obtained under voltage clamp condition using the AP in A and PCL=2 s. **C**. Upper panel: Steady-state activation (act_{ss}) and inactivation ($inact_{ss}$) curves of $I_{Ca,L}$. The red curve is the act_{ss} with 5 mV left-shift. Middle and lower panels: $I_{Ca,L}$ and $[Ca]_i$ before and after a 5 mV left-shift of $I_{Ca,L}$ steady-state activation curve under the same voltage clamp condition as in B. **D**. AP, $I_{Ca,L}$, and $[Ca]_i$ under free running condition (paced with PCL=2 s). The parameters are the same as in C. Note that under AP clamp conditions, 5 mV shift in act_{ss} has very small effect on $I_{Ca,L}$ and $[Ca]_i$ but under free running condition, EADs occur and the changes of $I_{Ca,L}$ and $[Ca]_i$ are large. The normal control model was used in panels A and B, and the L-type Ca channel open probability was increased (the same as in Fig.1 in the main text) in panels C and D.

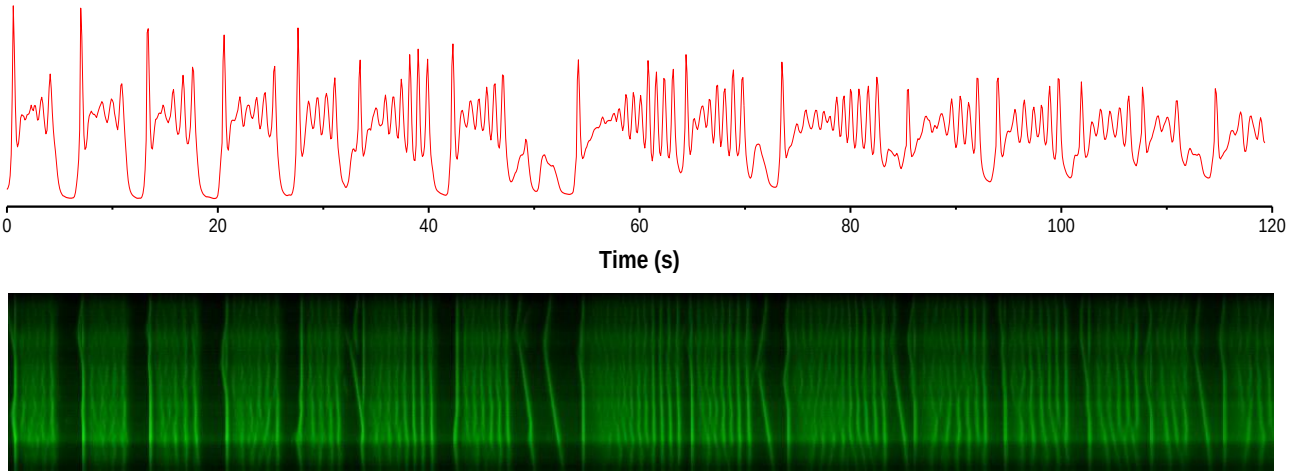

Fig.S5. The entire optical recording from which Fig.6B in the main text (from 40 s to around 72 s) was taken.

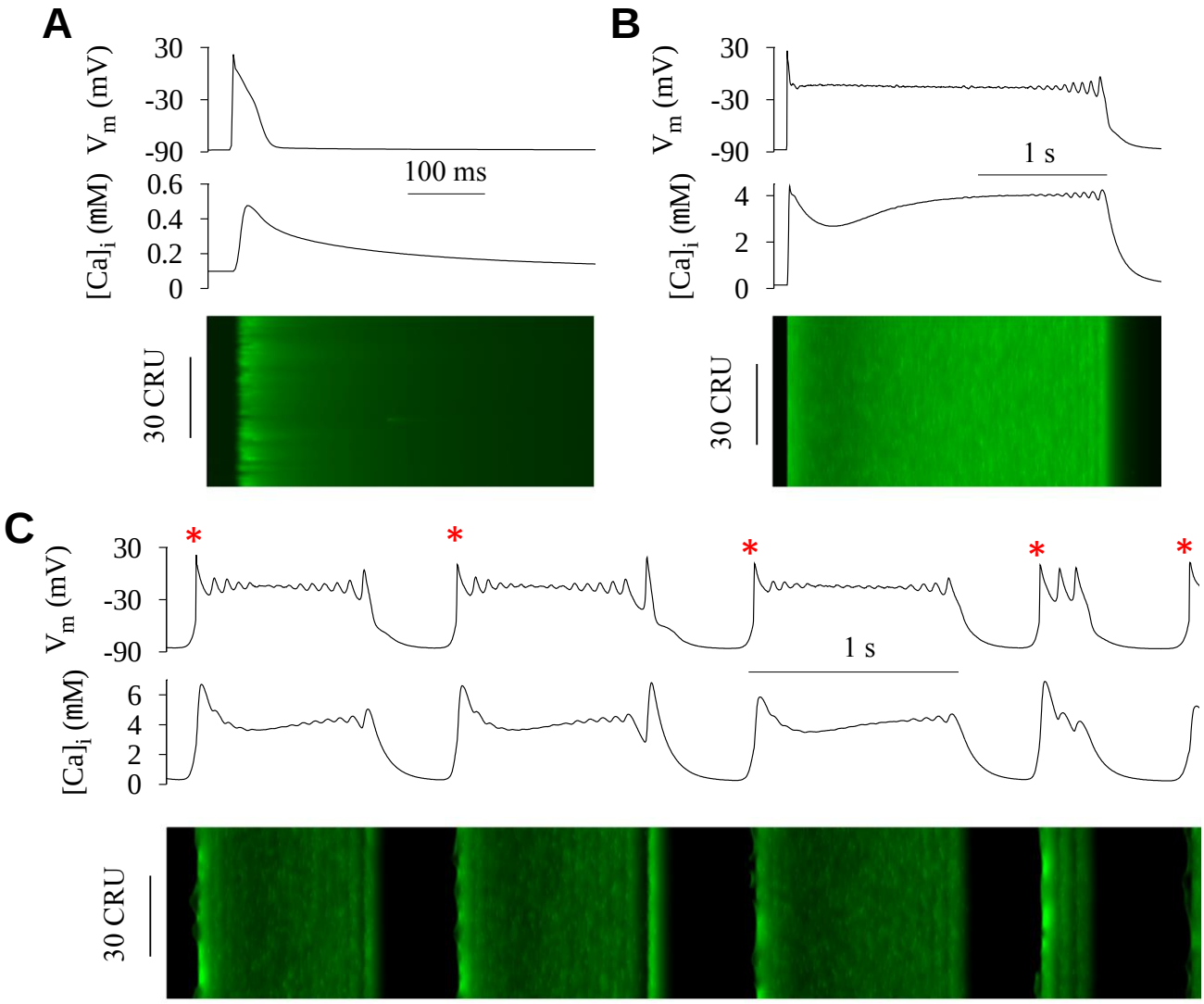

Fig.S6. Complex EAD-DAD dynamics in a mouse ventricular model. A. Time traces of voltage, whole cell averaged $[Ca]_i$ and the corresponding line scan for control conditions. PCL = 1 sec, and $[Ca]_o$ = 1 mM. **B**. pacing-induced EADs. $[Ca]_o$ = 2.7 mM and the maximum conductance of I_{NaL}=2.7 pA/pF. **C**. Spontaneous APs (indicated by asterisk) and EADs due to spontaneous Ca release. $[Ca]_o$=2.7 mM, the maximum conductance of I_{NaL}=1.2 pA/pF, with doubled the RyR leakiness, increased SERCA activity increased by 50%, and L-type Ca current by 50%. The mouse ventricular cell model were based on the model by Morrotti et al (5), as described in detail in the online supplemental text. The changes in B and C from control were under the assumption that Ca overload causes CaMKII activation which causes the corresponding changes to late I_{Na}, $I_{Ca,L}$, RyR, and SERCA.

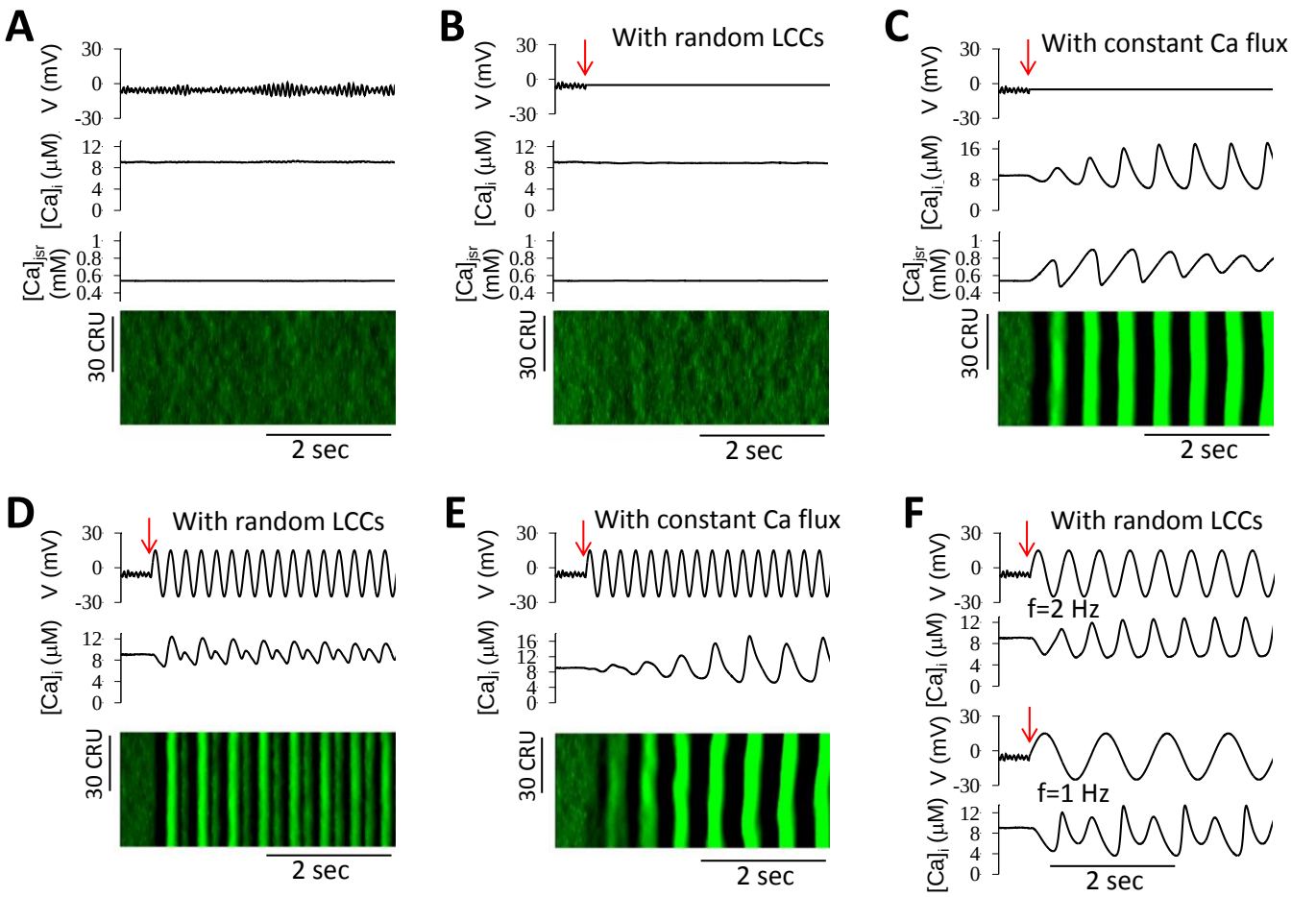

Fig.S7. **Interactions of voltage oscillations and Ca oscillations during repolarization failure**. Shown are voltage, $[Ca]_i$, and $[Ca]_{jsr}$ versus time, and line scan of $[Ca]_i$. The arrow in each case indicates the time when voltage clamp started. The parameters are the same as in Fig.1A in the main text but Ca overload ($[Ca]_o$=5 mM) with $[Na]_i$=10 mM and 7 mV left-shift in act_{ss} of $I_{Ca,L}$. **A**. The free-running voltage case in which repolarization failure occurs. **B**. Constant voltage clamp with normal LCCs present in CRUs. **C**. Same as B, but with a constant uniformly distributed $I_{Ca,L}$. **D**. Sinusoidal voltage clamp ($V(t)=A\sin 2\pi ft$ with A=20 mV and f=4 Hz) with normal LCCs present in CRUs. **E**. Same as D but with a constant uniformly distributed $I_{Ca,L}$. **F**. Voltage and $[Ca]_i$ versus time for a sinusoidal voltage clamp with normal LCCs present in CRUs, at different driving frequencies. Upper two panels: f=2 Hz. Lower two panels: f=1 Hz.

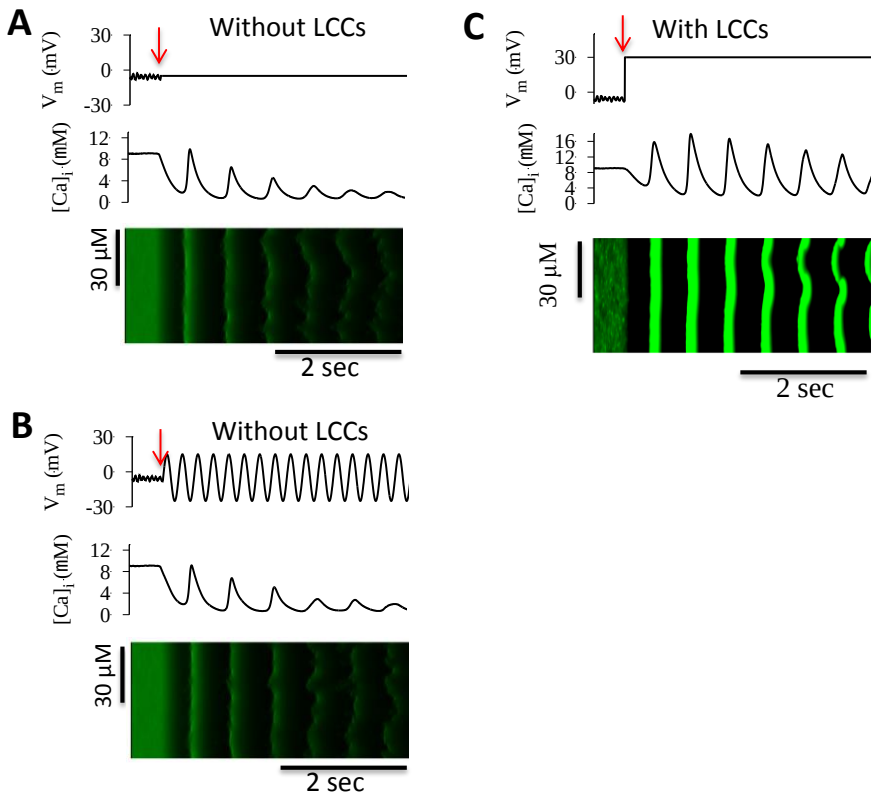

Fig.S8. Ca oscillations under different voltage clamp conditions (same as Fig.S7). **A** and **B**. The LCCs were removed without a constant Ca flux for compensation as in Fig.S7. Although the overall Ca decreased, the oscillations maintained. **C**. The LCCs were present, but the voltage was clamp at a higher value so that the LCCs are mostly inactivated to allow Ca oscillations to occur.

Interactions between voltage and Ca cycling during the long AP plateau (Detailed description of Figs.S7 and S8)

To explain the observation shown in the experiments in Fig.6 and the corresponding simulation in Fig.7 in the main text, in which no Ca oscillations (or very small fluctuations) in the long plateau phase but oscillations occur during the EAD phase, we carried out simulations (Figs.S7 and S8) by clamping the voltage during the AP plateau, so that we could observe the intrinsic underlying Ca cycling dynamics. We chose a parameter setting in which repolarization failure occurred such that voltage during the plateau remained around ~-5 mV, as illustrated in Fig.S7A. When no voltage clamp was imposed, voltage and whole-cell Ca exhibited small but irregular oscillations, and $[Ca]_i$ remained high. The line scan of Ca shows a random spatiotemporal pattern. We hypothesized that the random spatiotemporal pattern of Ca release under these conditions was likely to be related to the random openings of LCCs producing a random spatial pattern of Ca release sites during the plateau. To investigate how random opening of LCCs affects Ca oscillations, we carried out the following voltage clamp simulations. After starting each simulation from identical initial conditions, we imposed at a certain time point (arrow) either a voltage clamp to a constant voltage (Figs.S7B-C) or a voltage oscillation around the mean voltage (Figs.S7D-F).

When the voltage was held constant to promote random unsynchronized LCC openings, the whole-cell Ca and line scan (Fig.S7B) were very similar to the free-running case of repolarization failure (Fig.S7A). However, if LCCs were removed from the CRUs such that they could no longer trigger Ca sparks directly, and

were replaced by a uniformly-distributed constant Ca flux of the same magnitude as the LCC current so as to maintain the same cellular Ca level, a clear well-organized oscillation pattern immediately developed, as seen in the whole-cell Ca and the line scan (Fig.S7C). Even if the LCCs were removed without replacing them with a uniformly distributed constant Ca flux, Ca oscillations still developed immediately, but subsequently decreased in amplitude as the cellular Ca level declined due to the reduction in Ca entry (Fig.S8). Alternatively, if the voltage was held at a higher voltage to completely inactivate the LCCs, similar Ca oscillations occurred (Fig.S8).

If, instead of holding voltage constant during the plateau, a sinusoidal voltage clamp was imposed, the random spatiotemporal pattern of Ca sparks was replaced by a Ca oscillation pattern at the same frequency as the voltage oscillation (Fig.S7D), but with an alternating pattern. If the LCCs were removed and substituted by an equivalent constant Ca flux (Fig.S7E), however, the Ca oscillations did not alternate and exhibited an oscillation pattern virtually identical to that for the constant voltage case (Fig.S7C). However, now the periodic Ca oscillations were decoupled from the voltage oscillations, such that the frequencies of Ca and voltage oscillations were completely different. Fig.S6F shows $[Ca]_i$ for different oscillating frequencies of voltage with LCC intact (as in Fig.S7D). As the voltage oscillation frequency decreased, Ca alternans disappeared and $[Ca]_i$ developed a regular pattern (Fig.S7F, upper trace). However, if the driving frequency was decreased further, an alternating Ca oscillation pattern occurred again (Fig.S7F, lower trace).

These simulations demonstrate the following. When voltage is constant or nearly constant (Fig.S7B), the openings of the LCCs are random and uniform in space and time, resulting in random firings of CRUs in space and time. Therefore, at any time point, a spatially random portion of CRUs have yet to recover from their preceding firing. This random distribution of refractory CRUs reduces the likelihood that excitable CRUs activated by random openings of their LCCs or RyRs will be able to recruit neighboring CRUs and synchronize their refractory periods as required to generate an organized Ca oscillation. This is similar to the mechanism described in our previous study (2) showing that Ca waves and oscillations are emergent properties of the CRU network which strongly depend on CRU recruitment. On the other hand, when the LCCs are removed and replaced by an equivalent Ca flux (Fig. S7C), the number of randomly-firing CRUs causing dispersion of CRU refractoriness are reduced. This allows more effective recruitment to occur, which synchronizes the CRUs for organized Ca oscillations.

For the cases in which voltage oscillates (Figs. S7D-F), fewer LCCs are available for opening at high voltages but more are available at low voltages, and thus the voltage oscillation causes synchronous opening and closing of LCCs, resulting in synchronous firing of the CRUs, accounting for the organized Ca release patterns shown in Fig.S7D. However, if the driving frequency is fast so that the CRUs have not completely recovered from their previous firing, Ca alternans results, similar to the refractoriness mechanism of Ca alternans caused by rapid pacing with a free-running AP (16). When the driving frequency became slower so that CRUs had time to fully recover between oscillations, Ca alternans disappeared (Fig.S7F, upper traces). At even slower driving frequencies (Fig. S7F, lower traces), spontaneous synchronous CRU firings occurred between two pacing beats, resulting in a spontaneous beat followed by a voltage-driven beat, which is another type of Ca alternans.

References

1. Orth, P. M. R., J. C. Hesketh, C. K. H. Mak, Y. Yang, S. Lin, G. N. Beatch, A. M. Ezrin, and D. Fedida. 2006. RSD1235 blocks late INa and suppresses early afterdepolarizations and torsades de pointes induced by class III agents. Cardiovasc. Res. 70:486-496.
2. Nivala, M., C. Y. Ko, M. Nivala, J. N. Weiss, and Z. Qu. 2012. Criticality in intracellular calcium signaling in cardiac myocytes. Biophys. J. 102:2433-2442.
3. Liu, G. X., B. R. Choi, O. Ziv, W. Li, E. de Lange, Z. Qu, and G. Koren. 2012. Differential conditions for early after-depolarizations and triggered activity in cardiomyocytes derived from transgenic LQT1 and LQT2 rabbits. J. Physiol. 590:1171-1180.
4. Spencer, C. I., S. Baba, K. Nakamura, Ethan A. Hua, Marie A. F. Sears, C.-c. Fu, J. Zhang, S. Balijepalli, K. Tomoda, Y. Hayashi, P. Lizarraga, J. Wojciak, Melvin M. Scheinman, K. Aalto-Setälä, Jonathan C. Makielski, Craig T. January, Kevin E. Healy, Timothy J. Kamp, S. Yamanaka, and Bruce R. Conklin. 2014. Calcium Transients Closely Reflect Prolonged Action Potentials in iPSC Models of Inherited Cardiac Arrhythmia. Stem Cell Reports 3:269-281.
5. Morotti, S., A. G. Edwards, A. D. McCulloch, D. M. Bers, and E. Grandi. 2014. A novel computational model of mouse myocyte electrophysiology to assess the synergy between Na+ loading and CaMKII. J. Physiol. 592:1181-1197.
6. Goldhaber, J. I., L. H. Xie, T. Duong, C. Motter, K. Khuu, and J. N. Weiss. 2005. Action potential duration restitution and alternans in rabbit ventricular myocytes: the key role of intracellular calcium cycling. Circ. Res. 96:459-466.
7. Rae, J., K. Cooper, P. Gates, and M. Watsky. 1991. Low access resistance perforated patch recordings using amphotericin B. J. Neurosci. Methods 37:15-26.
8. Puisieux, F. L., M. M. Adamantidis, B. M. Dumotier, and B. A. Dupuis. 1996. Cisapride-induced prolongation of cardiac action potential and early afterdepolarizations in rabbit Purkinje fibres. Br. J. Pharmacol. 117:1377-1379.
9. Xie, L.-H., F. Chen, H. S. Karagueuzian, and J. N. Weiss. 2009. Oxidative Stress-Induced Afterdepolarizations and Calmodulin Kinase II Signaling. Circ. Res. 104:79-86.
10. Chang, M. G., C. Y. Chang, E. de Lange, L. Xu, B. O'Rourke, H. S. Karagueuzian, L. Tung, E. Marban, A. Garfinkel, J. N. Weiss, Z. Qu, and M. R. Abraham. 2012. Dynamics of Early Afterdepolarization-Mediated Triggered Activity in Cardiac Monolayers. Biophys. J. 102:2706-2714.
11. Collins, T. J. 2007. ImageJ for microscopy. BioTechniques 43:25-30.
12. Restrepo, J. G., J. N. Weiss, and A. Karma. 2008. Calsequestrin-mediated mechanism for cellular calcium transient alternans. Biophys. J. 95:3767-3789.
13. Luo, C. H., and Y. Rudy. 1994. A dynamical model of the cardiac ventricular action potential: I. simulations of ionic currents and concentration changes. Circ. Res. 74:1071-1096.
14. Rush, S., and H. Larsen. 1978. A practical algorithm for solving dynamic membrane equations. IEEE Trans. Biomed. Eng. 25:389-392.
15. Tian, T., and K. Burrage. 2004. Binomial leap methods for simulating stochastic chemical kinetics. J. Chem. Phys. 121:10356-10364.
16. Qu, Z., M. Nivala, and J. N. Weiss. 2013. Calcium alternans in cardiac myocytes: Order from disorder. J. Mol. Cell. Cardiol. 58:100-109.